

JGR Space Physics

RESEARCH ARTICLE

10.1029/2020JA028510

Special Section:

Early Results from the
Global-Scale Observations of the
Limb and Disk (GOLD) Mission

Key Points:

- Nighttime plasma bubble/depletions are observed at three longitude sectors with different separation of the geomagnetic and geographic equators
- The occurrence rate and time of occurrence for the months of November 2018 and March 2019 are different at different longitudes
- The growth rate of Rayleigh-Taylor instability is computed assuming empirical vertical drifts. Outputs do not explain all the observations

Correspondence to:

C. Martinis,
martinis@bu.edu

Citation:

Martinis, C., Daniell, R., Eastes, R., Norrell, J., Smith, J., Klenzing, J., et al. (2021). Longitudinal variation of postsunset plasma depletions from the global-scale observations of the limb and disk (GOLD) mission. *Journal of Geophysical Research: Space Physics*, 126, e2020JA028510. <https://doi.org/10.1029/2020JA028510>

Received 24 JUL 2020
Accepted 12 DEC 2020

Longitudinal Variation of Postsunset Plasma Depletions From the Global-Scale Observations of the Limb and Disk (GOLD) Mission

C. Martinis¹ , R. Daniell², R. Eastes³ , J. Norrell¹, J. Smith⁴, J. Klenzing⁴ , S. Solomon⁵ , and A. Burns⁵ 

¹Center for Space Physics, Boston University, Boston, MA, USA, ²Ionospheric Physics Consulting, Stoughton, MA, USA,

³Laboratory for Atmospheric and Space Physics, University of Colorado, Boulder, CO, USA, ⁴NASA Goddard Space Flight Center, ITM Physics Laboratory, Greenbelt, MD, USA, ⁵NOAA-SEC and CIRES, University of Colorado, Boulder, CO, USA

Abstract The Global-scale Observations of the Limb and Disk (GOLD) mission, launched in 2018, aims to investigate the low latitude ionosphere from a geostationary orbit at 47.5°W. It uses two identical spectrometers measuring the wavelength range from 134.0 to 163.0 nm. The configuration of the Earth's magnetic field shows that the largest offset between geographic and geomagnetic equators occurs in the longitude sectors sampled by GOLD. In an attempt to investigate the longitude dependence of the occurrence rate and time of onset of plasma bubbles, or plasma depletions, GOLD data were separated in three sectors: 65°–55°W, 50°–40°W, and 10°W–0°. Observations of the nighttime emissions in 135.6 nm on November 2018 and March 2019 show plasma depletions occurring very frequently at these longitudes. The growth rate of the Rayleigh-Taylor instability was computed at these longitudes under similar low solar activity conditions, assuming an empirical model of upward plasma drifts. The time and value of the maximum growth rates obtained cannot always explain the observations. On average, the observed occurrence rate of plasma depletions is high, with a maximum of 73% (observed during November 2018 at ~45°W). Most of the depletions observed in November at 45°W and 60°W occur within 1 h after sunset. When compared with the November 2018 observations, depletions in March 2019 occur at later times.

Plain Language Summary The Global-scale Observations of the Limb and Disk (GOLD) mission was launched in 2018 onboard a communication satellite. It measures nighttime emissions at 135.6 nm wavelength from a geostationary orbit at 47.5 W. Partial disk scans at different longitudes, selected to investigate how the configuration of the Earth's magnetic field affect the data, are studied for the months of November 2018 and March 2019. Occurrence rate of plasma depletions and the local time of occurrence are investigated. Model outputs for the growth rate of the Rayleigh-Taylor instability, the process responsible for the generation of the plasma depletions, are used to explain the observations.

1. Introduction

The Global-scale Observations of limb and disk (GOLD) mission, launched in 2018 uses two identical spectrometers measuring from 134.0 to 163.0 nm. This study focuses on the nighttime measurements using 135.6 nm data. The main production mechanism of this emission in the nighttime F region ionosphere is the radiative recombination of electrons and atomic Oxygen ions, O⁺,



where O^{*} and hν represent excited oxygen atoms and the recombination photons, respectively. The excited O^{*} atoms emit photons at 135.6, 130.4, 102.7, 98.9, and the 91.1 nm continuum from recombination into the ground state of O, O(³P). The 135.6 nm emissions result from the electric dipole transition



This transition consists of a doublet, ($^5S_2 \rightarrow ^3P_2$) and ($^5S_2 \rightarrow ^3P_1$). Further details on the different physical processes on the production and transport of the 135.6 nm photons in the ionosphere can be found in Qin et al. (2015).

Previous 135.6 nm global scale observations were performed by the Imager for Magnetopause-to-Aurora Global Exploration (IMAGE) satellite launched in March 2000. During spring 2002, the FUV imager was able to obtain a clear view of the northern airglow arc from the evening terminator to postmidnight local times. This viewing geometry allowed the study of the properties of the equatorial ionization anomaly (EIA) from March 2002 to early June 2002. The observations took place during high solar activity and the satellite measured strong crests of the EIA and significant variability (Immel et al., 2006; Sagawa et al., 2005). The IMAGE/FUV nighttime images have shown localized reductions in the brightness of equatorial airglow arcs. The decrease in airglow brightness is caused by depletions in plasma density or plasma bubbles associated with equatorial spread F irregularities (Kelley, 1989). Another instrument measuring in 135.6 nm was the Global Ultraviolet Imager (GUVI) on board of the Thermosphere Ionosphere Mesosphere Energetics and Dynamics (TIMED) spacecraft. When studying the occurrence rate of plasma bubbles GUVI data showed very low values (less than 5%) during solar minimum conditions (Comberiate & Paxton, 2010). This result appears to be an artifact due to the sensitivity threshold of the GUVI instrument in imaging mode and the low electron densities during solar minimum.

Thus when GOLD was launched, during a deep low solar minimum, it was uncertain whether the weak ionosphere during this period would produce sufficient emission for detection of plasma bubbles. Eastes et al. (2019) showed that GOLD not only clearly detected the equatorial ionization anomaly, but also significant day-to-day variability in its characteristics and a high occurrence rate of plasma bubbles/depletions associated with equatorial spread-F. Equatorial Spread-F is the descriptive name for the associated phenomenon observed in ionosonde data once the instability is well developed. The Rayleigh-Taylor instability is the driving mechanism for plasma bubble formation and the associated airglow depletions (Kelley, 1989).

A number of studies have investigated the variation of the structure of the EIA in different longitudinal sectors (Abdu, 2005). Studies have shown that the displacement between the geographic and the geomagnetic equators is one of the important factors that affect the behavior of the low latitudinal ionosphere. Based on total electron content (TEC) data from beacon satellite observations, the variation of the location and strength of the EIA crests in both hemispheres has been studied extensively for the American Sector (Basu et al., 2009), and many reports have been published for the Asian sector as well (Sunda & Vyas, 2013; Zhang et al., 2009). It was found that, besides the local time dependency, the strength and the latitudinal location of the EIA crests exhibit seasonal and solar cycle dependencies. In addition, the north-south asymmetries of EIA, both in magnitude and in latitudinal location have been revealed and ascribed to the effects of the trans-equatorial neutral wind and the location of the subsolar point.

Similar observations of longitudinal variations of plasma bubble occurrence have been reported. Burke et al. (2004a) compared DMSP and ROCSAT-1 observations of plasma bubbles during March-April 2000 and 2002. Plasma bubble occurrence was significantly smaller than expected near the west coast of South America. Gentile et al. (2006) showed the longitude dependence of plasma bubbles as observed by DMSP satellites. Costa et al. (2014) analyzed data from the Communications/Navigation Outage Forecasting System (C/NOFS) planar Langmuir probe (PLP) instrument and found that the highest probability of occurrence of plasma bubbles or irregularities was in the South American East sector for most combinations of geophysical parameters. For most longitude sectors, with the exception of the Pacific Ocean, the probability of occurrence reached minimum values during the June solstice.

The climatology of plasma bubbles occurrence indicates that, during equinox seasons, all longitudes show high level of activity. During December solstice high levels of activity are found in the American-Atlantic Ocean sector, with maximum occurrence rate in Eastern Brazil-Western Atlantic Ocean. In the Central Pacific sector, the highest level of activity is found during the June solstice. Aarons (1993) used in situ satellite and scintillation data to investigate the global behavior of equatorial irregularities, and the climatological pattern was confirmed.

Several studies have attempted to find the parameter (or parameters) responsible for the longitudinal variations observed. The alignment of the solar terminator with magnetic field lines is a major cause of the

seasonal and longitudinal variations in plasma bubble occurrence (Tsunoda, 1985). A large latitudinal separation of the crests of the EIA indicates a strong upward $E \times B$ drift, which also increases the growth rate of the Rayleigh-Taylor instability, γ_{RT} (Huang & Hairston, 2015). Batista et al. (1986) compared upward drifts at equatorial stations Fortaleza (38°W) and Huancayo (75°W) and concluded that the differences observed could be explained by the different magnetic declinations and thermospheric winds at the two sites. Burke et al. (2004b) attributed the longitudinal differences observed in the plasma bubbles occurrence to changes in E region conductance that are produced by varying B field magnitude with respect to longitude that affect radiation belt electrons and their loss cone distribution. Using ROCSAT-1 data Fejer et al. (2008) showed that the largest upward drifts were observed during Equinox and December solstice near the American sector and that the longitudinal variations of the evening prereversal velocity peaks during December and June solstice are anticorrelated, an indication of the importance of conductivity effects on the electrodynamics of the equatorial ionosphere. Yizengaw and Groves (2018) presented a review of the longitudinal variations of ionospheric irregularities. C/NOFS ion drift meter (IVM) data averaged from 2010–2013 for longitude intervals of 7° showed very clear longitudinal variability, which was stronger with larger drifts in the American and West Atlantic Ocean sectors, in particular during December solstice and March equinox (similar to the results by Fejer et al., 2008). The smallest postsunset drifts occurred in the 11.5°W longitude bin. This is consistent with the longitudinal variability of the dayside equatorial electrojet (EEJ) observations using magnetometers (Anderson et al., 2009; England et al., 2006). The importance of the longitudinal variation of forcing from below through the propagation of gravity waves was also stressed. Paznukhov et al. (2012) investigated the longitudinal occurrence of plasma bubbles and L band (GPS) scintillations over equatorial Africa. The results were adequately explained by the alignment of the solar terminator and local geomagnetic field. While plasma bubbles and scintillations were primarily observed during equinox, there were longitudinal differences showing that ~15°W the most intense, longest lasting, and highest scintillation occurrence rate in-season.

For the first time, we have the capability to measure simultaneously from a single location multiple longitude sectors on the same night for an extended period of time. In this paper we focus on three longitude sectors where the geomagnetic equator is found at different geographic latitudes and investigate characteristics of plasma depletions like occurrence rate and time of onset.

2. Instrumentation

The GOLD instrument is a dual-channel, spectral imager that measures the Far Ultraviolet (FUV) spectrum of Earth's upper atmosphere from geostationary orbit at 47.5°W. Each independent channel has a scan mirror, interchangeable slits, and an imaging detector that provides spectral information at spatial locations along the entrance slit. More details are described in Eastes et al., (2017). At equatorial and low latitudes, GOLD samples the upper atmosphere to the west near Western South America and to the east near Western Africa longitude sectors. The GOLD instrument in nighttime mode is used to provide images of the equatorial and low latitude ionosphere in 135.6 nm. The independent channels, Channels A and B, can observe either hemisphere with a 15 min cadence. To increase the signal-to-noise ratio (SNR) the nighttime mode scans only a portion of the disk during the 15 min. The low-resolution slit (~0.35 nm) is also used to further increase the instrumental response and the observing time at each location is more than doubled by scanning only ~45° of longitude (instead of full disk images), near sunset for most scans, while maintaining a cadence of 15 min per scan.

The details for the observation sequence for this work are as follows. Between 20:10 and 23:10 UT, Channel B is in night mode and alternates between the Northern and Southern Hemispheres. Between 23:10 and 23:55 UT (00:25 UT after December 19, 2018), both channels are in night mode and Channel A scans the Northern Hemisphere, while Channel B scans the Southern Hemisphere. Observations are made at a constant angular resolution that corresponds to ~90 km spatial resolution in the east-west and north-south directions for near nadir observations.

The initial nighttime scan occurs at 20:10 UT centered at ~5°W. Until December 19, 2019 the last nighttime scan occurred at 23:55 UT and covered the 65°–50°W longitude sector. After that date, two more scans were added, and the final sequence samples the 75°–60° longitude sector at 00:25 UT. After the 00:25 UT scan the instrument goes into safe mode to avoid sun light.

Table 1

Sunset and ESF Times for Three Different Longitudes for the Months of November and March.

	Sunset time (UT)						ESF time (UT)	
	1 Nov	30 Nov	<Nov>	1 Mar	31 Mar	<Mar>	<Nov>	<Mar>
5°W 10°N	18:35	18:36	18:35	19:08	19:08	19:08	19:35	20:08
45°W 0°	21:25	21:32	21:28	21:53	21:45	21:49	22:28	22:49
60°W 10°S	22:37	22:50	22:43	23:00	22:42	22:51	23:40	23:51

Columns labeled <Nov> and <Mar> represent the monthly average times.

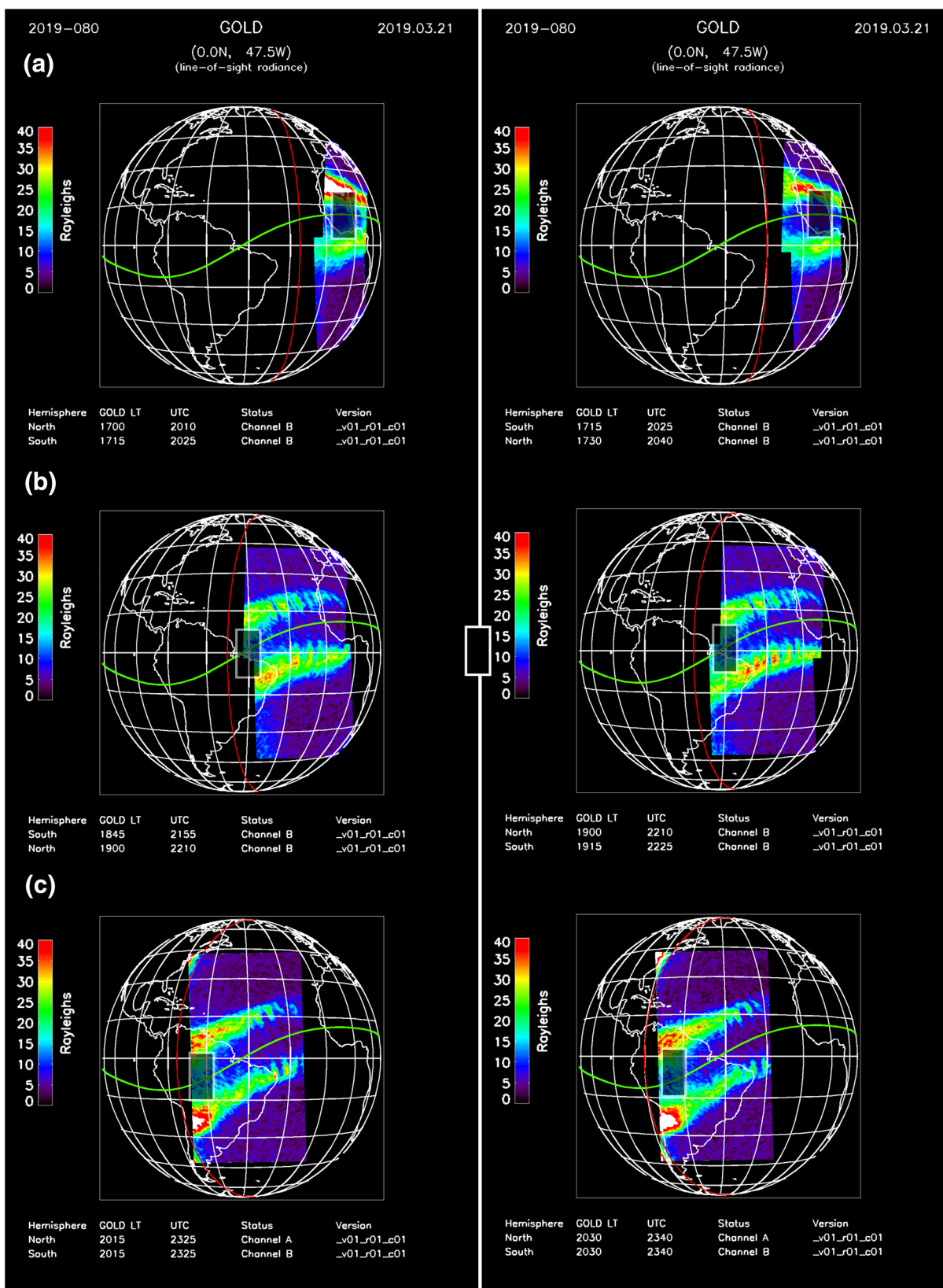
3. Postsunset Observations

Almost every night from mid-October 2018 to mid-April 2019 had airglow structures visible between ~20:00 and 00:25 UT. The airglow structures consist of bright east-west elongated bands in both hemispheres away from the magnetic equator, which are associated with the high electron density regions of the northern and southern crests of the EIA and plasma bubbles or depletions piercing through them. All the cases had plasma bubbles embedded in the crests of the EIA. Entering the month of May, very low structuring was observed in the entire American sector (from ~30° to 80°W). In this study we focus on postsunset observations on November 2018 and March 2019.

Figure 1 shows a composite image of several partial disk scans during March 21, 2019. The top panel (A) shows the initial scans at 20:10 and 20:25 UT (left) and 20:25 and 20:40 UT (right). The shaded boxes show the region covering ~0–10°W. The green curve represents the magnetic equator, and the red vertical line shows the location of the sunset terminator. In these very first scans, bubbles can be seen piercing through the equatorward edges of the crests of the equatorial ionization anomaly. Subsequent scans cover more western regions and by 21:55 and 22:10 UT GOLD is scanning the region between 40° and 50°W. Another scan at 22:25 UT is used to detect the bubbles in this sector (middle panel (B)). Panel (C) shows scans with Channels A and B at 23:25 UT (left) and 23:40 UT (right), covering the 55°–65°W sector. The crests of the EIA are seen closer to the magnetic equator with bubbles piercing through them. Well-developed, high latitude bubbles are seen to the east (corresponding to the depleted regions sampled in the scans from panel (B)). During this night, the three longitude sectors all contained plasma depletions. By repeating this procedure for all the nights in November 2018 and March 2019 we compute the time when plasma depletions, or decreases in 135.6 nm brightness, are observed in a given scan and the occurrence rate at a given longitude sector. The original choice for the western longitude sector was 65°–75°W, where magnetic declination is almost zero, but due to the original scanning sequence this option did not provide enough data for the analysis.

The Rayleigh-Taylor instability needs a few growth periods to evolve into large-scale perturbations and reach altitudes of ~600 km at the magnetic equator apex. Typical values for large growth rates are $\sim 8 \times 10^{-4}$ – $1 \times 10^{-3} \text{ sec}^{-1}$ (Sultan, 1996), so growth times ($1/\gamma_{\text{RT}}$) are ~20–15 min. We can assume that after ~1 h (3–4 growth times) the instability due to a Rayleigh-Taylor process is fully developed. Then, the resulting plasma bubble is able to reach heights at the magnetic equator that will cause the brightness decreases that are attributed to bubbles piercing through the crests of the EIA in the GOLD data. Under some conditions, additional forcing is present and growth rates are faster (Huba & Liu, 2020), so the time for full development can be as short as 30 min.

As we will show later, the growth rate of the RTI maximizes right after sunset, so it is important to specify sunset times at the locations analyzed. Table 1 shows the sunset times at 100 km at the three representative longitudes and 0° magnetic latitude. Average times for March are similar (around 18:50 LT) while for November, earlier sunset time occurs at 5°W in the northern hemisphere (19:15 LT) and later time occurs at 60°W in the southern hemisphere (19:40 LT). In general GOLD observes bubbles at magnetic latitudes higher than $\sim \pm 10^\circ$. This implies that they are reaching a minimum apex height of ~500 km, meaning that if they are generated at 250–300 km, one expects them reach 500 km after ~1–1.5 h. Thus, the last two columns in Table 1 indicate at what time plasma bubbles should be observed at different longitudes (assuming they are fully developed 1 h after sunset).



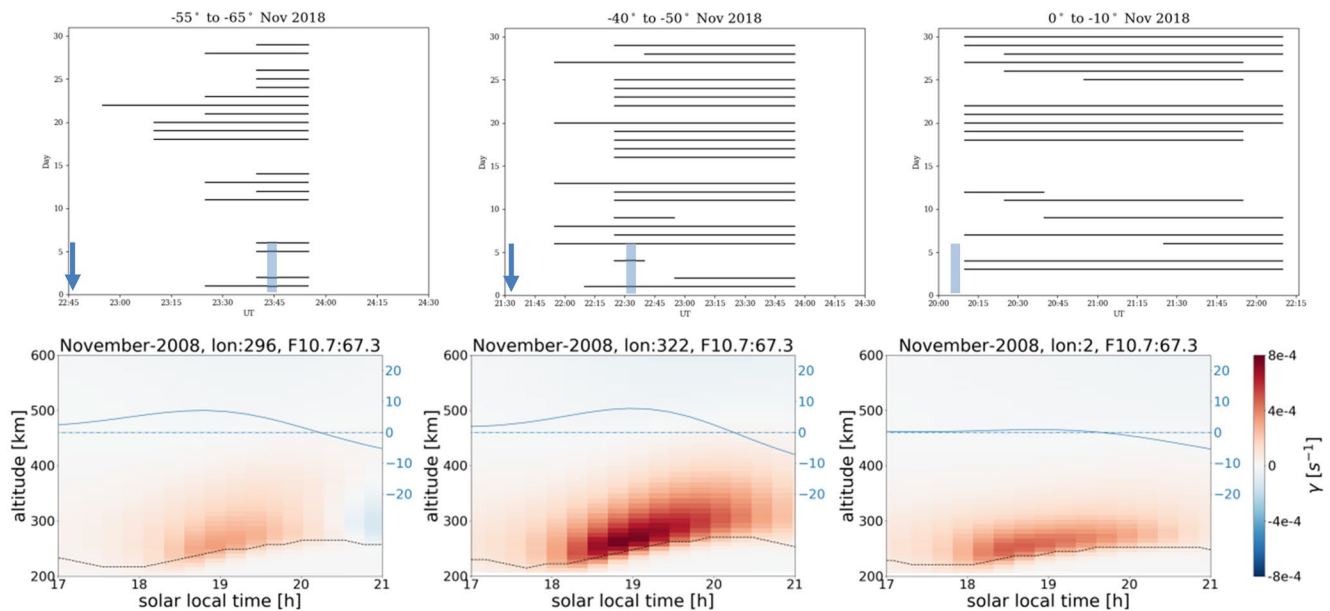


Figure 2. (Top) plasma bubbles detected at different longitude sectors during November 2018. The arrows show local sunset time. The light blue rectangles indicate 1 h after sunset for the left and center panels, and 1.5 h after sunset for the right panel. (Bottom) Rayleigh-Taylor instability growth rate at similar longitudes during low solar activity conditions in the 17–21 local time period. The blue curves show the empirical upward drifts used to calculate the growth rate. The maximum growth rate is obtained at 322°E (38° W).

The top row in Figure 2 shows the time of occurrence of plasma bubbles as a function of the day on November 2018. The left panel shows the data at 60°W, the center panel at 45°W, and the right panel at 5°W. The blue arrows indicate the time of sunset at 100 km. The light blue rectangles are centered on 1 h after sunset for the left and center panels. The right panel has only the rectangle showing the time 1.5 h after sunset. At the bottom, model results of the growth rate of the Rayleigh-Taylor instability are shown for similar longitudes during low solar activity ($F_{10.7} = 67$). The blue lines indicate the upward plasma drifts obtained from the Fejer-Scherliess empirical model (Scherliess & Fejer, 1999). The growth rates are computed from the output generated by the combined grown and sami2py python modules (Klenzing & Smith, 2019; Smith & Klenzing, 2020). It uses the SAMI2 model (Huba et al., 2000) that includes NRLMSISE-00 (Picone et al., 2002) to obtain neutral densities and temperature, EUVAC (Richards et al., 1994) to obtain the EUV flux, HWM-14 (Drob et al., 2015) to obtain the neutral wind velocity, and IGRF (Thebault et al., 2015) to obtain the magnetic field geometry and magnitude. The values for the Fejer-Scherliess model of ionospheric vertical plasma drift are obtained here from the NRLMSISE-00 model primarily due to its preexisting integration into the SAMI2 model. SAMI2 is run for a representative day in each season and longitude sector for 24 h at approximate 15 min intervals. Being driven by empirical models, the resultant modeled ionosphere is representative of the average monthly behavior of the winds, ion drifts, etc. Subsequently, flux-tube integrated growth rates, as described by Sultan (1996), are calculated for all flux tubes in each of the 15 min intervals from the SAMI2 output.

GOLD data show that in the eastern Brazil-Western Atlantic sector (Figure 2, middle panel, top row), bubbles are observed earlier and more frequently (73%) than at the other two longitude sectors. The occurrence rate computation is based on the number of days of the month on which bubbles were observed. The Western South-America sector (left panel in the top row) also shows a relatively high occurrence rate

Figure 1. (a) Initial scans with Channel B at 20:10 and 20:25 UT (left) and 20:25 and 20:40 UT (right). The shaded boxes cover the longitude sector ~0–10°W. The green curve represents the magnetic equator. The red line indicates the sunset terminator. In these initial scans bubbles can be seen piercing the equatorward edges of the crests of the equatorial ionization anomaly; (b) Channel B scans between 21:55 and 22:10 UT (left) and between 22:10 and 22:25 UT (right). The shaded boxes now are over the sector ~40–50°W. Well developed, high latitude bubbles are seen to the east (they correspond to the initial depleted regions sampled in the scans from panel (A)); (c) scans with Channels A and B at 23:25 UT (left) and 23:40 UT (right). The crests of the EIA seem to be closer to the magnetic equator and bubbles are seen piercing them. Again, notice the well-developed, high latitude bubbles to the east (initial depleted regions sampled in the scans from panel (A)). During this night plasma bubbles were detected in the three longitude sectors.

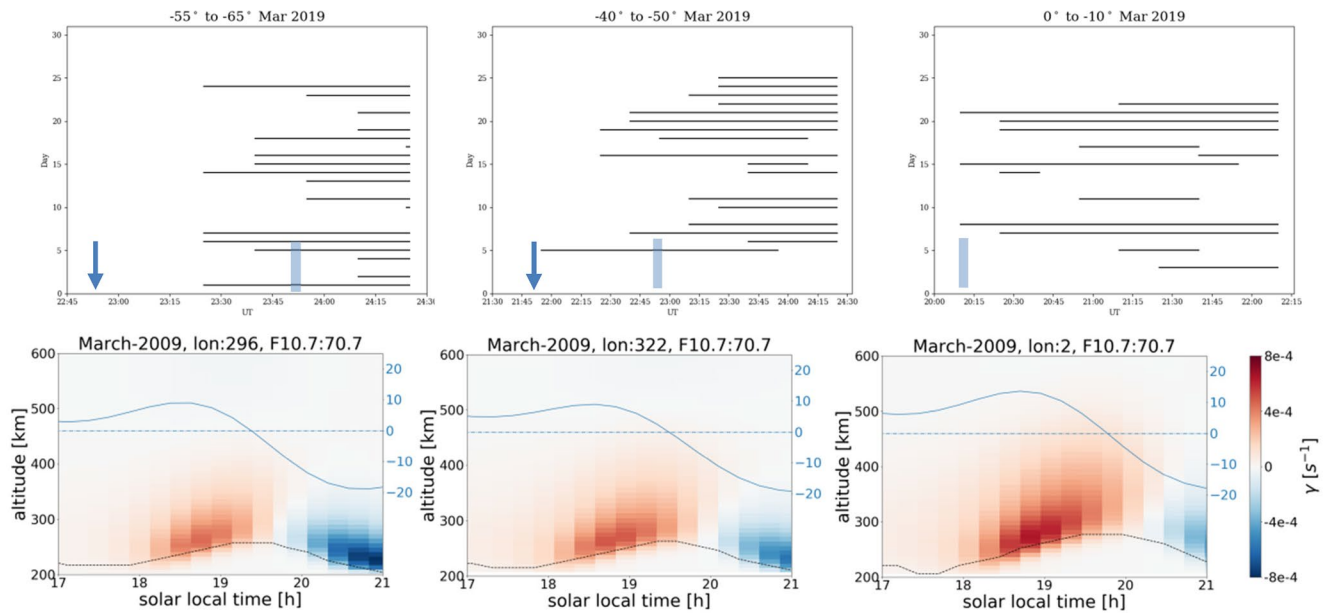


Figure 3. Similar to Figure 2, but for March 2019. The light blue rectangles in each panel at the top indicate 1 h after sunset. Computed growth rates (bottom) are smaller with maximum values obtained at 2°E. GOLD data at this longitude sector (top right panel) show that plasma bubbles are observed later in time.

(63%) while the Western African sector (right panel in the top row) also shows the latest onset time (it takes longer for plasma bubbles to be observed) and the lowest occurrence rate (60%). The growth rate calculations (bottom row) clearly show that the largest growth rate occurs at 322°E (38°W, middle panel), meaning that at this longitude sector plasma bubbles should be observed earlier and more frequently during this month, in agreement with the observations. The left and middle panels in the top row also show that 4 and 5 nights, respectively, have bubbles occurring just 30 min after sunset, indicating nights with very large growth rates not only where the maximum growth rate is obtained, but also in Western South America. The first scan in the Western African sector occurs at 20:10 UT and by this time GOLD is showing bubbles on 12 nights. The remaining six nights show bubbles first observed more than 2 h after sunset, in agreement with the low growth rates shown at the right panel in the bottom row. Sunset local time is earlier at 5°W, meaning that one should expect bubble detection occurring sooner at this longitude sector, but we are not seeing this.

Figure 3 shows similar plots but for the month of March 2019. The behavior observed at the three longitude sectors is similar, with overall reduced occurrence rates, 58% in the West-American sector, 55% in Brazil-West Atlantic, and 42% in the East-Atlantic-West-African sector. At 60°W, half of the bubbles is observed within 1 h after sunset, with five occurring just 30 min after sunset. The lowest computed growth rate is at this longitude sector, meaning that plasma bubbles should develop and be observed the latest. While the growth rate in the African sector seems to be relatively large, GOLD observations indicate a lower occurrence rate and bubbles appearing later in time. This inconsistency could be due to limitations in the growth rate calculations or in the observing geometry. As pointed out by Eastes et al. (2019) the African region is the least favorable for identification of depletions due to the off nadir viewing geometry (looking ~40° to the east). Nevertheless, GOLD is still observing a relatively high occurrence rate, 42% of the time. In the 45°W sector, the results are similar to the ones observed at 60°W with almost half of the bubbles occurring within 1 h after sunset.

The results from Figures 2 and 3 show that, on average, the occurrence rate of plasma bubbles is high, with a maximum of 73% (observed on November 2018 at 45°W). Most of the bubbles in the American and West-Atlantic sectors observed in November occur within 1 h after sunset, while in the African-East Atlantic sector most of the bubbles are observed ~1.5–2 h after sunset.

4. Discussion and Summary

Strong upward drift near the magnetic equator is considered to be a main driver for the occurrence plasma bubbles and well developed equatorial ionization anomaly (Fejer et al., 1999). If these plasma bubbles/depletions are detected earlier at a given longitude, one can hypothesize that the equatorial vertical drifts at this longitude are stronger (how fast the depletions reach a given magnetic latitude at a fixed height can be related to how fast plasma bubbles move upward near the magnetic equator). Consequently, while the growth rate depends on multiple parameters (Sultan, 1996), to first order the GOLD observations can be used to examine longitudinal variations in the behavior of vertical plasma drifts. A hint of this was presented in the work by Eastes et al. (2019), who showed examples of variable location of the crests when observed at different longitudes. In order to quantify this variability, GOLD data have been separated in three longitude sectors, with the magnetic equator $\sim 10^\circ$ south of the geographic equator (at $\sim 60^\circ\text{W}$), at the geographic equator (at $\sim 45^\circ\text{W}$), and $\sim 10^\circ$ north of the geographic equator (at $\sim 5^\circ\text{W}$). The selection of these sectors is based on the available data for the periods investigated. Ideally we would have chosen the western sector to be centered at $\sim 75^\circ\text{W}$, when magnetic declination is almost zero and the magnetic equator shows the maximum offset with respect to the geographic equator, but the latest scan only reached 65°W . One of the parameters that varies significantly at these locations is the magnetic declination, that goes from around -15° near 60°W to $\sim -20^\circ$ at $\sim 45^\circ\text{W}$, to almost 0° at $\sim 5^\circ\text{W}$. Data from November 2018 to March 2019 were compared. Given the similarity in magnetic declination at 60° and 45°W we are not expecting significant differences at these two longitude sectors. Geomagnetic activity was quiet, with the exception of small storms occurring on November 4–6 (Dst ~ -51 nT), and March 16–17 (Dst ~ -40 nT) and no abnormal behavior was observed during these dates. GOLD observations show that there are differences in the behavior of plasma bubbles at the longitude sectors examined.

During November of 2018 the highest occurrence rates and earliest plasma bubbles observation occur in the sectors covering 45° and 60°W . More specifically, these two sectors show that most of the plasma bubbles appear within 1 hour after sunset. This result suggests that the Tsunoda's hypothesis of having the solar terminator and B field aligned is the dominant mechanism. In the 0 – 10°W range, the plasma bubbles appear later when compared with the other two sectors. The maximum growth rate is smallest at 296°E , Western South America (a growth period ~ 50 min) and largest at 38°E , Eastern Brazil (growth period ~ 20 min), but we see no difference in the timing of the detection by GOLD. The times for the maximum γ_{RT} is $\sim 18:50$ LT ($22:50$ UT) in Western South America, and $\sim 18:30$ LT ($\sim 18:30$ UT) at 2°E , the East Atlantic region, values that are basically the sunset times at the magnetic equator in these longitudes.

During March 2019 occurrence rates are similar at the three longitude sectors, and depletions are observed later when compared with November 2018. Calculations of the growth rate of the RTI at different longitudes do not support the observations. The times when plasma bubbles are detected by GOLD agree with the occurrence rates results, i.e., earlier times correlate with higher occurrence rates. Specifically, the East Atlantic/Western Africa sector ($\sim 5^\circ\text{W}$) shows that only 3 out of 13 nights bubbles are observed within 1 h after sunset, while in the other two sectors half of the bubbles are detected within 1 h after sunset. At all three longitude sectors a significant portion of the bubbles are observed 1.5 h after sunset, meaning that, on average, it takes longer for plasma bubbles to evolve when compared with the November observations. The time of maximum γ_{RT} is similar at the three sectors: $\sim 18:36$ LT. The maximum growth rate does not vary significantly, but it is smallest at $\sim 60^\circ\text{W}$ (growth period ~ 35 min), and largest near 5°W (growth period ~ 25 min). However, near 5°W bubbles are observed less frequently and later when compared with the other two sectors, meaning that the modeled growth rate cannot explain the March observations and that factors different than the Tsunoda's B field/terminator alignment condition are affecting the observations. In addition, even when the computed growth rate near 60°W is the smallest, half of the bubbles are observed within 1 h after sunset and a few just 30 min after sunset.

The goal of this paper was to understand if this different longitudinal behavior could be the result of the different configuration of the geomagnetic field at these longitudes, the different values of the intensity of the equatorial magnetic field, a combination of both effects, or more complex interactions involving other factors. The GOLD data presented here do not find significant differences between the sectors centered at 45° and 60°W meaning that these two sectors might be too close to detect differences due to the configuration and intensity

of the magnetic field, confirming Tsunoda's hypothesis involving B field and solar terminator alignment. But observations during March in the western Africa sector imply that other mechanisms are affecting the results.

In summary, the data analyzed here show high occurrence rate of plasma depletions at the three longitude sectors in both months. The time of occurrence varies with the month and longitude sector, with earlier times observed in November 2018 at the two sectors centered at 45° and 60 °W. Calculated growth rates using empirical plasma drifts do not match all the observations, in particular when analyzing the 5°W longitude sector.

Since the longitudinal variability of plasma bubbles occurrence depends on the terms involved in the growth rate of the RTI, like neutral winds, plasma drifts, E and F region conductivities, additional diagnostics should be included in future studies. GOLD data, from its unique perspective of observing a large region from a fixed longitude, will help to understand how the thermosphere-ionosphere response to these different forcing terms changes with longitude.

Data Availability Statement

The data used in this study are available at the GOLD Science Data Center (<http://gold.cs.ucf.edu/search/>) and at NASA's Space Physics Data Facility (<https://spdf.gsfc.nasa.gov>).

Acknowledgments

This research was supported by NASA Contract 80GSFC18C0061 to the University of Colorado and subcontract to Boston University. NCAR is also supported by the National Science Foundation. This work uses the SAMI2 ionosphere model written and developed by the Naval Research Laboratory. Work by J. Smith and J. Klenzing is supported by the Heliophysics Innovation Fund at Goddard Space Flight Center.

References

- Aarons, J. (1993). The longitudinal morphology of equatorial F-layer irregularities relevant to their occurrence. *Space Science Reviews*, 63, 209–243. <https://doi.org/10.1007/BF00750769>
- Abdu, M. A. (2005). Equatorial ionosphere–thermosphere system: electrodynamics and irregularities. *Advances in Space Research*, 35, 771–787. <https://doi.org/10.1016/j.asr.2005.03.150>
- Anderson, D., Araujo-Pradere, E., & Scherliess, L. (2009). Comparing daytime, equatorial E × B drift velocities and TOPEX/TEC observations associated with the 4-cell, non-migrating tidal structure. *Annales de Geophysique*, 27(7), 2861–2867. <https://doi.org/10.5194/angeo-27-2861-2009>
- Basu, Su., Basu, S., Huba, J., Krall, J., McDonald, S. E., Makela, J. J., et al. (2009). Day-to-day variability of the equatorial ionization anomaly and scintillations at dusk observed by GUVI and modeling by SAMI3. *Journal of Geophysical Research*, 114, A04302. <https://doi.org/10.1029/2008JA013899>
- Batista, I. S., Abdu, M. A., & Bittencourt, J. A. (1986). Equatorial F region vertical plasma drifts: Seasonal and longitudinal asymmetries in the American sector. *Journal of Geophysical Research*, 91(A11), 12055–12064. <https://doi.org/10.1029/JA091iA11p12055>
- Burke, W. J., Huang, C. Y., Gentile, L. C., & Bauer, L. (2004b). Seasonal-longitudinal variability of equatorial plasma bubble occurrence. *Annales Geophysicae*, 22, 3089–3098. <https://doi.org/10.5194/angeo-22-3089-2004>
- Burke, W. J., Gentile, L. C., Huang, C. Y., Valladares, C. E., & Su, S. Y. (2004a). Longitudinal variability of equatorial plasma bubbles observed by DMSP and ROCSAT-1. *Journal of Geophysical Research*, 109, A12301. <https://doi.org/10.1029/2004JA010583>
- Comberiate, J., & Paxton, L. J. (2010). Global Ultraviolet Imager equatorial plasma bubble imaging and climatology, 2002–2007. *Journal of Geophysical Research*, 115, A04305. <https://doi.org/10.1029/2009JA014707>
- Costa, E., Roddy, P. A., & Ballenthin, J. O. (2014). Statistical analysis of C/NOFS planar Langmuir probe data. *Annales Geophysicae*, 32, 773–791. <https://doi.org/10.5194/angeo-32-773-2014>
- Drob, D. P., Emmert, J. T., Meriwether, J. W., Makela, J. J., Doornbos, E., Conde, M., et al. (2015). An update to the Horizontal Wind Model (HWM): The quiet time thermosphere. *Earth and Space Science*, 2(7), 301–319. <https://doi.org/10.5194/angeo-32-773-2014>
- Eastes, R. W., McClintock, W. E., Burns, A. G., Anderson, D. N., Andersson, L., Codrescu, M., et al. (2017). The Global-scale Observations of the Limb and Disk (GOLD) mission. *Space Science Reviews*, 212(1–2), 383–408. <https://doi.org/10.1007/s11214-017-0392-2>
- Eastes, R. W., Solomon, S. C., Daniell, R. E., Anderson, D. N., Burns, A. G., & England, S. L. (2019). Global-scale observations of the equatorial ionization anomaly. *Geophysical Research Letters*, 46, 9318–9326. <https://doi.org/10.1029/2019GL084199>
- England, S. L., Maus, S., Immel, T. J., & Mende, S. B. (2006). Longitudinal variation of the E-region electric fields caused by atmospheric tides. *Geophysical Research Letters*, 33, L21105. <https://doi.org/10.1029/2006GL027465>
- Fejer, B. G., Jensen, J. W., & Su, S.-Y. (2008). Quiet time equatorial F region vertical plasma drift model derived from ROCSAT-1 observations. *Journal of Geophysical Research*, 113, A05304. <https://doi.org/10.1029/2007JA012801>
- Fejer, B. G., Scherliess, L., & de Paula, E. R. (1999). Effects of the vertical plasma drift velocity on the generation and evolution of equatorial spread F. *Journal of Geophysical Research*, 104(A9), 19859–19869. <https://doi.org/10.1029/1999JA900271>
- Gentile, L. C., Burke, W. J., & Rich, F. J. (2006). A climatology of equatorial plasma bubbles from DMSP 1989–2004. *Radio Science*, 41, RS5S21. <https://doi.org/10.1029/2005RS003340>
- Huang, C., & Hairston, M. R. (2015). The postsunset vertical plasma drift and its effects on the generation of equatorial plasma bubbles observed by the C/NOFS satellite. *Journal Geophysical Research: Space Physics*, 120, 2263–2275. <https://doi.org/10.1002/2014JA020735>
- Huba, J., Joyce, G., & Fedder, J. A. (2000). SAMI2 is another model of the Ionosphere (SAMI2): A new low-latitude ionosphere model. *Journal of Geophysical Research*, 105(10), 23035–23053. <https://doi.org/10.1029/2000JA000035>
- Huba, J. D., & Liu, H.-L. (2020). Global modeling of equatorial spread F with SAMI3/WACCM-X. *Geophysical Research Letters*, 47, e2020GL088258. <https://doi.org/10.1029/2020GL088258>
- Immel, T. J., Sagawa, E., England, S. L., Henderson, S. B., Hagan, M. E., Mende, S. B., et al. (2006). Control of equatorial ionospheric morphology by atmospheric tides. *Geophysical Research Letters*, 33, L15108. <https://doi.org/10.1029/2006GL026161>

- Kelley, M. C. (1989). The Earth's ionosphere: Plasma physics and electrodynamics. In International Geophysics Series (Vol. 43). New York, NY: Academic Press.
- Klenzing, J., & Smith, J. (2019). *jklenzing/sami2py: Patch for initial release*. Zenodo Version v0.1.1. <http://doi.org/10.5281/zenodo.3066510>
- Paznukhov, V. et al. (2012). Equatorial plasma bubbles and L-band scintillations in Africa during solar minimum. *Annales de Geophysique*, 30, 675–682. <https://doi.org/10.5194/angeo-30-675-2012>
- Picone, J. M., Hedin, A. E., Drob, D. P., & Aikin, A. C. (2002). NRLMSISE-00 empirical model of the atmosphere: Statistical comparisons and scientific issues. *Journal of Geophysical Research*, 107(A12), 1–16.
- Qin, J., Makela, J. J., Kamalabadi, F., & Meier, R. R. (2015). Radiative transfer modeling of the OI 135.6 nm emission in the nighttime ionosphere. *Journal of Geophysical Research: Space Physics*, 120, 10116–10135. <https://doi.org/10.1002/2015JA021687>
- Richards, P. G., Fennelly, J. A., & Torr, D. G. (1994). Correction to “EUVAC: A solar EUV flux model for aeronomic calculations”. *Journal of Geophysical Research*, 99(A7), 13283.
- Sagawa, E., Immel, T. J., Frey, H. U., & Mende, S. B. (2005). Longitudinal structure of the equatorial anomaly in the nighttime ionosphere observed by IMAGE/FUV. *Journal of Geophysical Research*, 110, A11302. <https://doi.org/10.1029/2004JA010848>
- Scherliess, L., & Fejer, B. G. (1999). Radar and satellite global equatorial F region vertical drift model. *Journal of Geophysical Research*, 104(A4), 6829–6842. <https://doi.org/10.1029/1999JA900025>
- Smith, J., & Klenzing, J. (2020). *JonathonMSmith/growin: Beta (Version 0.1-beta.1)*. Zenodo. <http://doi.org/10.5281/zenodo.3678866>
- Sultan, P. J. (1996). Linear theory and modeling of the Rayleigh-Taylor instability leading to the occurrence of equatorial spread F. *Journal of Geophysical Research*, 101(A12), 26875–26891.
- Sunda, S., & Vyas, B. M. (2013). Local time, seasonal, and solar cycle dependency of longitudinal variations of TEC along the crest of EIA over India. *Journal of Geophysical Research: Space Physics*, 118, 6777–6785. <https://doi.org/10.1002/2013JA018918>
- Thébault, E., Finlay, C. C., Beggan, C. D., Alken, P., Aubert, J., Barrois, O., et al. (2015). International geomagnetic reference field: The 12th generation international geomagnetic reference field – The twelfth generation. *Earth, Planets and Space*, 67, 67–79. <https://doi.org/10.1186/s40623-015-0228-9>
- Tsunoda, R. T. (1985). Control of the seasonal and longitudinal occurrence of equatorial scintillations by the longitudinal gradient in integrated E region Pedersen conductivity. *Journal of Geophysical Research*, 90, 447–456. <https://doi.org/10.1002/2014EA000089>
- Yizengaw, E., & Groves, K. M. (2018). Longitudinal and seasonal variability of equatorial ionospheric irregularities and electrodynamics. *Space Weather*, 16, 946–968. <https://doi.org/10.1029/2018SW00198>
- Zhang, M., Wan, W., Liu, L., & Ning, B. (2009). Variability study of the crest-to-trough TEC ratio of the equatorial ionization anomaly around 120°E longitude. *Advances in Space Research*, 43, 1762–1769. <https://doi.org/10.1016/j.asr.2008.09.031>